Heliyon 10 (2024) e32793

Contents lists available at ScienceDirect

Heliyon

journal homepage: www.cell.com/heliyon

Research article

Effects of oxygen concentration on the corrosion behavior of high entropy alloy AlCoCrFeNi in simulated deep sea

Junwei Wang [a,b,*], Wenhui Wen [a], Fa Xie [a], Bo Wu [a,b], Yang Yang [a,b], Jun Cheng [c], Shilong Zhang [a], Xianhui Zhang [a,b,**]

[a] Xiamen Key Laboratory of Marine Corrosion and Smart Protective Materials, Department of Marine Engineering, Jimei University, Xia Men 361021, China
[b] Fujian Province Key Laboratory of Naval Architecture and Marine Engineering, Department of Marine Engineering, Jimei University, Xia Men 361021, China
[c] College of Mechanical and Energy Engineering, Jimei University, Xia Men 361021, China

ARTICLE INFO

Keywords:
Deep sea
Oxygen concentration
High entropy alloy
AlCoCrFeNi
Electrochemical corrosion

ABSTRACT

In light of the low dissolved oxygen concentration in the deep sea, the corrosion mechanisms of the high entropy alloy (HEA) AlCoCrFeNi in artificial seawater with varying oxygen concentrations (2.0, 4.0, 7.0 mg/L) were studied. As the oxygen concentration decreases, the alloy's free corrosion potential decreases, and at 2.0 mg/L, the corrosion rate is 421 times higher than that at 7.0 mg/L. The corrosion form transforms from pitting to uniform corrosion. The primary reasons for this are the passivation film is thin under low oxygen concentration conditions, as well as the preferential dissolution of the alloy elements Al and Ni due to their high activity and "local acidizing" properties, respectively. In designing a super corrosion-resistant high entropy alloy for use in the deep sea, it is advisable to avoid the use of element Al and to add Ni with caution.

1. Introduction

The deep sea is defined as the area with a depth greater than 500 m. Within the vast expanse, there is an abundance of resources such as oil, gas, combustible ice, and metal deposits, making it one of the prime fields for future resource exploitation [1,2]. However, the ocean is a harsh and complex corrosive environment that includes high salinity, high/low temperature, dissolved oxygen concentration differences, seawater velocity, and complex marine organisms, among other factors [3]. Compared to the shallow-sea environment, the deep sea has low dissolved oxygen concentration, high hydrostatic pressure, and low temperature [4]. The corrosion behaviors of marine equipment's metal structural components (such as gears, bearings, connecting rods, sliding rails of a submarine, deep sea oil/gas pipelines and oil drilling platforms, slush pumps, etc.) working in the deep sea are distinctly different from those in shallow-sea environments [5–8]. Starting in the 1960s, in-situ materials performance experiments in the deep sea at locations such as Port Winnipeg in California and the Indian Ocean [9,10], as well as in the South China Sea [4,11], have demonstrated that the dissolved oxygen concentration is the most significant factor affecting the corrosion rate of metals in deep sea environments [10,12,

---

[*] Corresponding author. Xiamen Key Laboratory of Marine Corrosion and Smart Protective Materials, Department of Marine Engineering, Jimei University, Xia Men 361021, China.

[**] Corresponding author. Xiamen Key Laboratory of Marine Corrosion and Smart Protective Materials, Department of Marine Engineering, Jimei University, Xia Men 361021, China.

E-mail addresses: wangjw86@163.com (J. Wang), zhangxianhui@jmu.edu.cn (X. Zhang).

https://doi.org/10.1016/j.heliyon.2024.e32793
Received 12 August 2023; Received in revised form 4 June 2024; Accepted 10 June 2024

13].

Although oxygen concentrations vary in different oceanic areas, the change tendencies are similar along the ocean depth: it decreases near the surface and then slightly increases [10,14]. In shallow-sea environments, the dissolved oxygen concentration is the highest (~7.0 mg/L) due to sea wave motion, contact with air, and photosynthesis by seaweed [4,10]. As the ocean depth increases, the dissolved oxygen concentration decreases because photosynthesis weakens and more oxygen is consumed by ocean animals. Generally, the oxygen concentration is the lowest (2.0–2.5 mg/L) near the ocean depth of 700 m [15]. As the depth further increases, the oxygen concentration increases slightly. This is due to cold, dense, oxygenated water sinking and convection in polar regions; and less oxygen is consumed by ocean animals [13].

There are two effects of dissolved oxygen on the corrosion behavior of a metal in deep sea environments. On one hand, except for magnesium (Mg), which has a very low potential, most metals' cathodic reactions in seawater are oxygen reduction reactions [13]. As the concentration of dissolved oxygen decreases, the corrosion rate also decreases. Therefore, in-situ performance experiments in deep sea environments have shown that the corrosion rates of low alloy steel (Ni–Cr–Mo–V) [13], martensitic steel, austenitic cast iron [10], and copper alloy (Cu - 32.55 % Zn) [16] are consistent with the dissolved oxygen concentration. In other words, the corrosion rates of these alloys decrease as the oxygen concentration decreases. Generally, those alloys are non-passivated alloy, and has high corrosion rate in sea water. For example, the corrosion rate of a medium carbon steel (a component of a nuclear reactor that sank in 1989) is 75 μm/y at a depth of 1655 m in the Southwest Norwegian Sea [17]. On the other hand, as the dissolved oxygen concentration decreases, the protective passivation film on the surface of a passivable alloy also reduces. This makes corrosion pitting more likely to nucleate. In-situ exposure testing of a 316SS at a depth of 3000 m in the South China Sea showed that the main forms of corrosion are pitting and crevice corrosion. As the exposure depth increases, the pitting depth and its diameter also increase. The corrosion rate of the 316SS at 3000 m depth is 2.5 times higher than that at shallow-sea depths. This is very dangerous for ocean equipment [18]. Certainly, the impact of hydrostatic pressure and temperature cannot be disregarded in the aforementioned in situ exposure testing in deep sea environments [3].

Human beings never stop innovating and exploring the unknown. In 2004, High Entropy Alloy (HEA) was introduced by Jien Wei Yeh et al. [19], which consists of five or more elements in a mole fraction ranging from 5 to 35 %. In addition to its excellent mechanical performance, due to the "cocktail effect", HEA containing elements such as Cr, Ni, and Al exhibits superior corrosion resistance compared to conventional stainless steel in solutions such as NaCl, HNO_3, HCl, and others [20–22]. Thanks to the "High entropy effect", HEA containing high concentrations of corrosion-resistant elements remains as a FCC or BCC phase without the formation of complex intermetallic compounds. Therefore, galvanic corrosion can be prevented in electrolyte solutions [21,22]. It is well known that the CoCrFeNi system HEAs were the earliest proposed and have been widely studied [19,23]. Yunzhu Shi et al. [24] reported that the tensile strength increases significantly after adding alloy element Al to the CoCrFeNi system. Additionally, with the increase of Al concentration, the AlxCoCrFeNi alloy exhibits good corrosion resistance in a 3.5 wt% NaCl solution due to the thicker passivation film thickness and more positive pitting potential. In simulated seawater (3.5 % NaCl solution), the High entropy alloy $AlNbTiZrSi_x$ exhibited higher passive current density, because the Zr_5Al_3 phase regions preferential corroded, and the addition of Si reduced passive film stability, which worsening corrosion resistance [25]. A High-entropy alloy film (~3 μm) of VAlTiCrSi was prepared by using the DC magnetron sputtering with the (V–Al–Ti–Cr–Si) spliced targets. In artificial sea-water, a passive film mainly composed of oxidation of V, Al, Ti, Cr and Si is formed, which can protect the sample from corrosion [26]. L. Xue et al. found the $Al_2Cr_5Cu_5Fe_{53}Ni_{35}$ is a single-phase, solid solution alloy with FCC crystal structure, similar to FeNi intermetallic compound. The alloy exhibits a better local corrosion resistance than conventional martensitic stainless steel UNS S40300 when temperature is below 60 °C in similar electrolytic environment [27]. A CoCrFeMnNi high-entropy alloy thin film was prepared on a Cu substrate by potentiostatic electrodeposition at various potentials in the DMF-CH_3CN organic system with $LiClO_4$ additive. The film has a good corrosion behavior in artificial seawater [28]. Dohyung Kim et al. for an offshore plant steel needs in deep sea, compared the microstructure and corrosion performance of high-entropy alloy and austenite and super duplex stainless steels in 3.5 % NaCl solution. It is found SDSS2507 has excellent corrosion resistance, but is unsuitable for use at low temperatures (in deep sea) owing to its low-temperature brittleness, the HEA FeCrNiCoMn exhibit low-temperature twinning and low corrosion-resistance, which can be used in the deep seas environment [29]. Yih-Farn Kao et al. [30] also reported that the hardness of $Al_xCoCrFeNi$ increases with the increase of x. When x approaches 1.0, the HEA exhibits a BCC structure, which has excellent hardness (~500 HV), yield strength (> 1360 MPa), and plasticity (~17 %) [30,31]. AlCoCrFeNi coatings have also been prepared using atmospheric plasma spraying (ASP) [32], high-velocity oxygen fuel (HVOF), and high-velocity air fuel (HVAF) [33], and their corrosion resistance in solutions such as NaCl an H_2SO_4 have been studied. Therefore, AlCoCrFeNi HEAs are the most promising materials as key components or coatings on inexpensive carbon steel surfaces used in ocean equipment. However, to our knowledge, the corrosion resistance of AlCoCrFeNi in a deep-sea environment has not been reported.

The study investigated the impact of dissolved oxygen concentration on the corrosion behavior of cast AlCoCrFeNi in a simulated South China Sea environment. The pH value (ranging from 7.4 to 8.0) and salinity (consistent with measured values of 3.43–3.44 % in the South China Sea) were maintained to mimic the actual conditions [4]. To isolate the single-factor effect of dissolved oxygen concentration on corrosion, the pressure (1 atm) and temperature (25 °C) of the corrosion system were kept constant. This research provides a theoretical foundation for designing alloys with superior corrosion resistance to meet the demands of deep-sea equipment.

2. Experiment

The HEA AlCoCrFeNi cast ingots, each weighing approximately 200g, were produced using a medium frequency induction melting furnace. Prior to casting, precise weighing of 40.0 g of electrolytically pure (> 99.9 %) raw Al, Co, Cr, Fe, and Ni particles was conducted using an electronic analytical balance with a precision of 0.1 mg (SOPTOP-FA2004, Shanghai Sunny Hengping Scientific

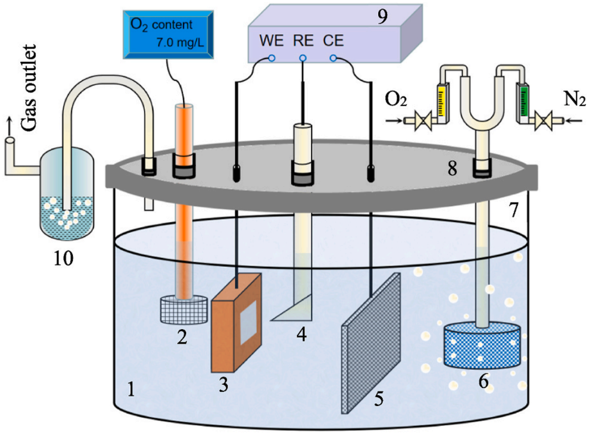

Fig. 1. Electrochemical corrosion test apparatus for simulating different oxygen concentration in deep sea environment, 1. Artificial seawater; 2. Dissolved oxygen concentration tester; 3. Work electrode; 4. SCE; 5. Counter electrode; 6. Dissolved oxygen concentration controller; 7. Electrolytic tank; 8. Electrolytic tank's cover; 9. Electrochemical workstation; 10. water seal.

Instrument Co., Ltd.). These particles were approximately 3 mm × 3 mm × 3 mm in dimension and were supplied by Beijing Jiaming Platinum Nonferrous Metal Co. Ltd. To minimize element content deviation caused by the ablation of active elements, an additional 1.0 g of elemental Al and Cr was added. The casting was conducted under an argon atmosphere. After the temperature of the ingot dropped to room temperature, the ingot was removed from the furnace and then cut into small blocks with dimensions of 10 mm × 10 mm × 3 mm using an electric discharge wire cutting machine (China Taizhou electric discharge wire Co. Ltd). All block samples were successively polished using 500#, 1000#, and 2000# SiC paper, then cleaned and dried.

To investigate the microstructure of the HEA sample, the polished samples were corroded using aqua regia ($HCl: HNO_3 = 3:1$). Subsequently, the microstructure and elemental analysis were conducted using a laser scanning confocal microscope (LSCM, KEYENCEVK-X250) and a scanning electron microscope equipped with an energy dispersive X-ray detector (SEM/EDS, Carl Zeiss Sigma500). It is important to emphasize that the as-cast HEA sample without etching was used to determine its elemental composition using EDS.

The samples utilized for the electrochemical property studies were connected to a wire and sealed with epoxy resin, except for a 1 cm^2 surface area that was exposed. The electrochemical corrosion test setup is illustrated in Fig. 1. A conventional three-electrode system was employed, with the reference electrode being a saturated calomel electrode (SCE), $E_{SCE} = E_{SHE} + 0.241$ V. The counter electrode used was a Pt net measuring 20 mm × 20 mm. The electrolytic tank was filled with 200 ml artificial seawater prepared according to ASTM-D1141 [34]. The pH level of the solution was adjusted to 7.8 by adding HCl solution. The dissolved oxygen concentration was controlled by adjusting the flow rates of O_2 and N_2. The gaps between the electrode/wire and the electrolytic tank cover were sealed to prevent oxygen from dissolving into the electrolyte from the air. The exhaust holes are sealed by water. During the experiment process, the oxygen concentration in artificial seawater was measured using a dissolved oxygen concentration meter (LEICI, JPB-607A). After the oxygen concentration is stable within the proposed range $c\pm0.1$ mg/L ($c = 7.0$ mg/L (shallow-sea), 4.0 mg/L, 2.0 mg/L (the lowest level in deep sea)) for 1 h, the work electrode immersed into the artificial seawater. The electrochemical parameters were evaluated using a multi-channel electrochemical workstation (Autolab M204). After the working electrode (sample) was allowed to corrode freely for more than 2 h, the electrochemical impedance spectroscopy (EIS) was conducted over a frequency range of 0.01 Hz–100 MHz under open circuit potential (OCP). The AC modulation amplitude was set at 10 mV. After the EIS testing was complete, the OCP value was re-measured. Once the values stabilized, the sample underwent a reduction treatment at a constant potential of −0.5 V vs. OCP to remove any oxide films that may have been present on its surface. Then the potentiodynamic polarization curve was then tested from −0.5 V to 1.5 V vs. OCP at a scanning rate of 1.0 mV/s. When the anode polarization current reached 0.5 mA/cm^2, the scanning direction was reversed. The corrosion rates of the alloy in artificial water were calculated using Tafel strong polarization region data. According to Faraday's law, the corrosion rate expressed in terms of corrosion depth, v (mm/y), is calculated as: $v = Mi_{corr}/nF\rho$. Here, M represents the relative atomic mass of the material (50.4 g/mol), i_{corr} denotes the corrosion current at the intersection of the extrapolated Tafel lines in the strong polarization region; n is the number of electrons gained or lost in the electrode reaction equation; F is Faraday's constant (96,485 C/mol); ρ stands for the material density (7.1 g/cm^3). Both M and ρ are calculated using the formulas $M = \sum A_iW_i$ and $\rho = \sum \rho_iW_i$, respectively." Where, A_i, W_i, and ρ_i represent the relative atomic mass, mass fraction (wt%) and the density of the ith component in the high-entropy alloy, respectively. Compared to the loss weight method, the electricity method has high test efficiency, but it also has a larger data error range [35]. And the following approximations were adopted: (1) Assuming that the mass transfer process in the strong polarization region is sufficiently fast, thus neglecting the concentration polarization in this region; (2) The corrosion rate was determined based on the assumption that uniform corrosion occurred in the sample. (3) The electrochemical equivalent, $C = 21.42$, of the high-entropy alloy is calculated using the following formula: $C = 1/\sum \frac{x_i}{C_i}$, where x_i and c_i is represent the mass fraction and the chemical equivalent of the ith element in the alloy, respectively. Three parallel samples were tested at each dissolved oxygen condition. During the electrochemical testing, O_2 and N_2 were continuously supplied to the

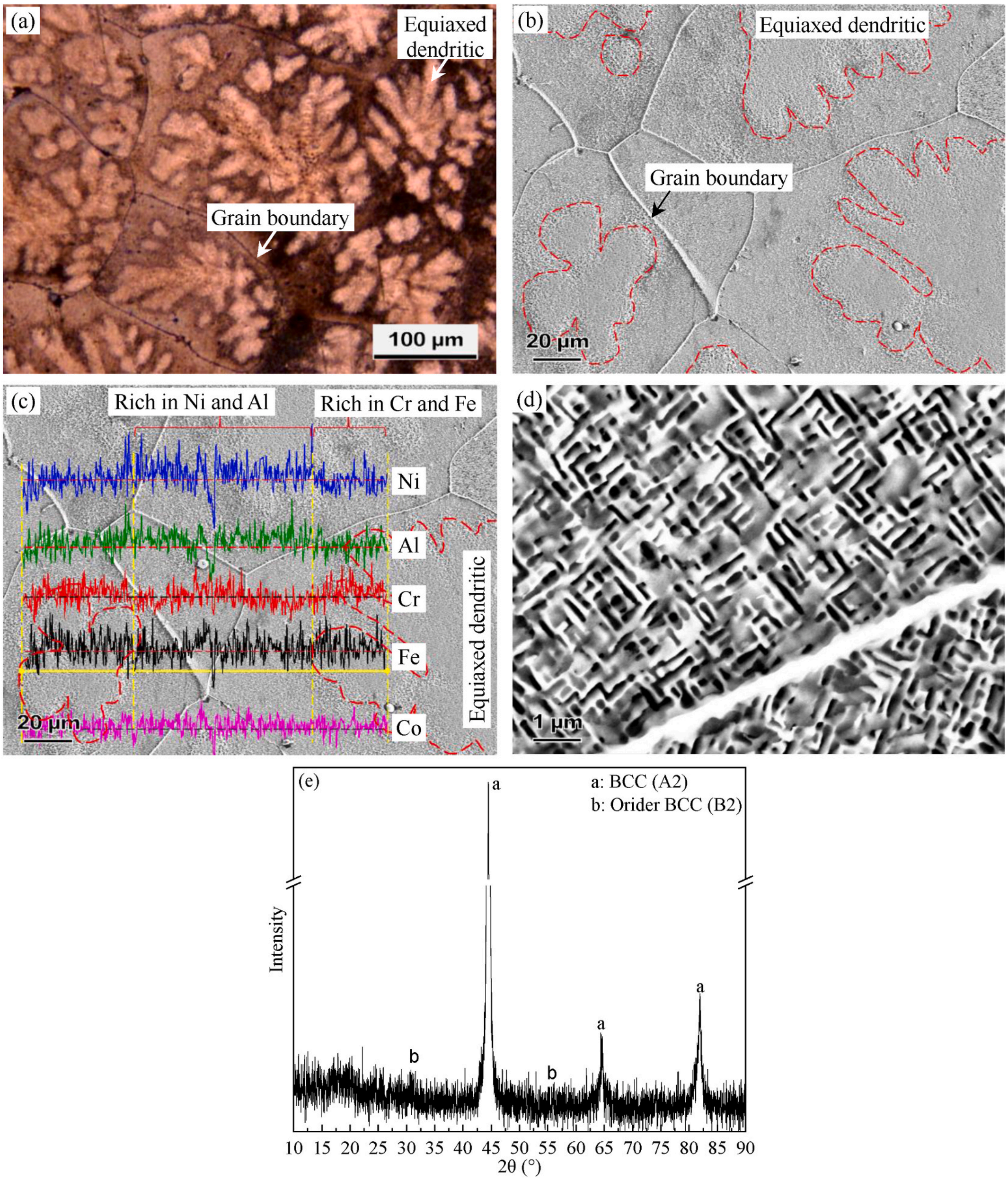

Fig. 2. Microstructure and composition of AlCoCrFeNi (a) LSCM metallographic picture; (b), (c), (d) high resolution SEM images with EDS (insert in (c)) and XRD analysis (e).

electrolyte, and the dissolved oxygen concentration was constantly monitored. To confirm the corrosion mechanism, electrochemical experimental data for pure metals (Al, Co, Cr, Fe, and Ni) were obtained using the same methods under specific conditions. In the deep-sea environment, in addition to dissolved oxygen content, changes in factors such as pressure, temperature, pH, and salinity can all affect the corrosion rate of metals. However, because this article only studies the influence of dissolved oxygen content, other parameters are set at constant values: pressure is 0.1 MPa, temperature is 25 ± 2 °C, pH is 7.8 (except for corrosion experiments on pure metals in acidic environments), and salinity is 3.43 %.

After the potentiodynamic polarization testing, the samples were immersed in deionized water and ethyl alcohol for 10 min each, then dried with N_2. The corroded sample surface was then analyzed using scanning electron microscopy/energy-dispersive X-ray spectroscopy (SEM/EDS).

Table 1
The mixing enthalpies of atom-pairs between each element for present alloys (kJ/mole) and pure metals' melting point [35].

	Cr	Fe	Co	Ni	Al	Melting point/°C
Cr	0	−1	−4	−7	−10	1907
Fe	/	0	−1	−2	−11	1538
Co	/	/	0	0	−19	1493
Ni	/	/	/	0	−22	1453
Al	/	/	/	/	0	660

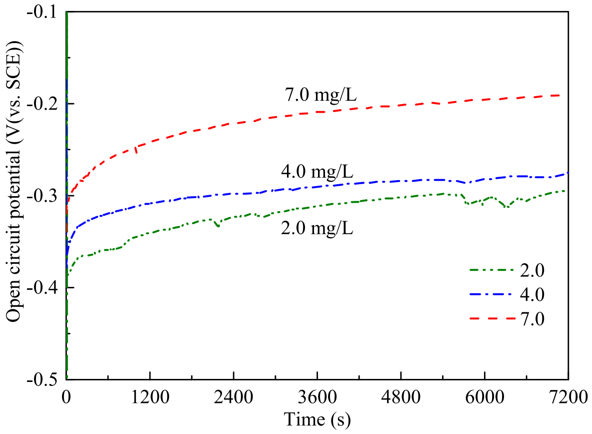

Fig. 3. OCP of the AlCoCrFeNi in artificial seawater with different oxygen concentration.

3. Results

3.1. Microstructure

The cast AlCoCrFeNi's microstructure taken by LSCM is presented in Fig. 2(a). The equiaxed dendrites can be clearly observed in polygonal block grains, indicating that their solidification temperature ranges are broader. The SEM images and the microstructure linear scanning results are showed in Fig. 2(b) and (c), respectively. The composition of the tested as-cast sample (without etching using aqua regia) is as follows (at %): Al: 18.9 ± 0.6 %, Co: 21.0 ± 1.5 %, Cr: 18.4 ± 0.3 %, Fe: 19.6 ± 0.5 %, and Ni: 21.1 ± 0.6 %. This composition is similar to the nominal composition of 20.0 at% for each element. The equiaxed dendritic protrude around the surface. The content of elements Al and Ni are slightly higher at the interdendrite than that in the dendrite.

The unique microstructure is associated with the negative mixing enthalpy of Ni–Al. As indicated in Table 1, the mixing enthalpy of Ni–Al is more negative compared to other elements [36]. During the initial stage of solidification, due to structural and energetic fluctuations, regions rich in Al–Ni and those rich in Fe–Cr emerge in the subcooled melt. The new grains first appear in the rich-Fe-Cr regions due to their higher melting point compared to the rich Al and Ni regions [37]. It has been reported [38] that there is significant lattice distortion when the element Al is added to HAE CoCrFeNi (FCC), as the atomic radius of Al is large. In comparison to the FCC structure, the BCC structure has a lower fill rate, which helps to relieve lattice distortion. Consequently, the first grains formed in the HEA (rich in Fe–Cr and containing Al) have a BCC structure. Certainly, some scholars believe that the element Al possesses a unique electronic structure, which facilitates the formation of bonds with transition metals that have an incomplete filling of electrons in their d-layer. The rich Al–Ni melts are squeezed into the dendrites, which are reminiscent of the Al–Ni phase. This phase exhibits an ordered BCC structure like the CsCl structure upon solidification [39]. The high-magnification SEM image of the microstructure, presented in Fig. 2(d), reveals a periodically arranged fine-scale structure with a width of approximately 100 nm. These structures are spinodal decomposition products, which have been previously reported in Refs. [30,40]. In a solid solution, the diffusion coefficient of component i is expressed as: $D_i = kTB_i\left(1 + \frac{\partial \ln \gamma_i}{\partial \ln c_i}\right)$. In the formula, k is the Boltzmann constant, T is the absolute temperature, B_i is the atomic mobility of component i, γ_i is the activity coefficient of component i in the solid solution, and c_i is the concentration of component i. When the thermodynamic factor $\left(1 + \frac{\partial \ln \gamma_i}{\partial \ln c_i}\right) < 0$, $D_i < 0$, indicating that diffusion proceeds in the same direction as the concentration gradient. This leads to uphill diffusion, resulting in the formation of phases with identical crystal structures but with periodic compositional fluctuations, a phenomenon known as spinodal decomposition. Through this process, an ordered BCC phase (B2 structure) and a disordered BCC phase (A2 structure) are formed. Their unit cell structures resemble the conventional BCC structure, but in the B2 structure, the atoms at the vertices differ from those at the body center, while the A2 atoms exhibit a disordered arrangement [41,42]. Reference [40] further analyzed these structures using transmission electron microscopy (TEM). The TEM

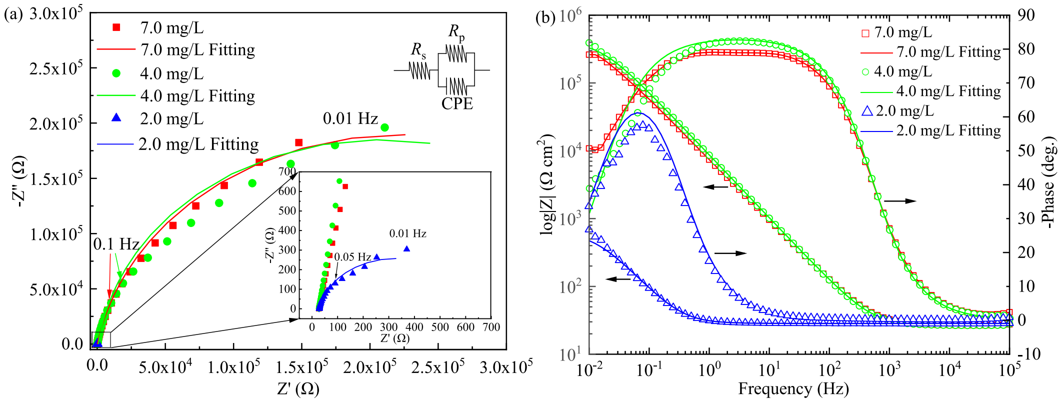

Fig. 4. EIS of the AlCoCrFeNi in the artificial seawater with different oxygen concentration, (a) Nyquist plot, (b) Bode plot.

Table 2
The main electrochemical parameters of the equivalent circuit

O_2 concentration/(mg/L)	R_s(Ω)	R_p(Ω)	Y_0(μMho*$S^θ$)	$θ$	$χ^2$
7.0	26.596	448.470	26.168	0.893	0.09
4.0	26.753	413.830	20.907	0.928	0.08
2.0	28.395	0.603	1.783×10^4	0.937	0.03

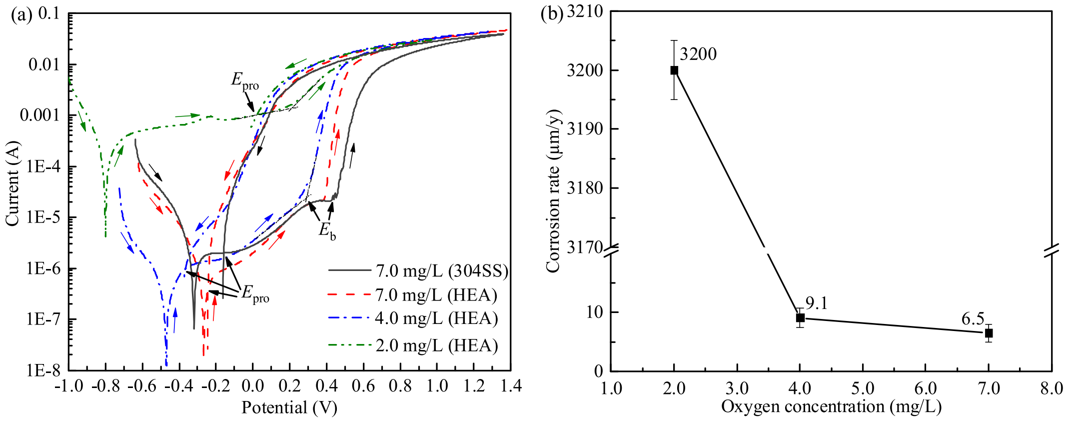

Fig. 5. Cyclic potentiodynamic polarization curves and corrosion rate of AlCoCrFeNi under the different oxygen concentration, (a) cyclic potentiodynamic polarization curves, (b) corrosion rate.

images revealed that the spinodal structure consists of an ordered BCC phase (B2 structure) and a disordered BCC phase (A2 structure). This finding is consistent with previous reports in Refs. [30–32,40]. But the elements Al and Ni are rich lightly at the interdendrite. After being corroded by the aqua regia, the interdendritic region was preferentially corroded due to the high activity of the alloy element Al, which was more susceptible to corrosion. So, the equiaxed dendritic can be found as shown in Fig. 2(a) and (b).

3.2. Electrochemical corrosion behavior

The sample's OCP under three different oxygen concentrations are showed in Fig. 3. The OCP reduces with the decreasing of the oxygen concentration.

The electrochemical impedance spectroscopy (EIS) data under three different oxygen concentrations are presented in Fig. 4. A simplified R–C equivalent circuit model was utilized to represent the electrochemical system's architecture, which is schematically illustrated in Fig. 4(a). The main electrochemical parameters are showed in Table 2. The solution resistance, denoted by R_s, exhibits minimal variations across the three oxygen concentration levels. This observation suggests that the oxygen concentration has minimal impact on the solution resistance. R_p is a film resistance. As shown in Table 2, the lower of the oxygen concentration, the lower of the R_p. It's worth noting that the R_p at the oxygen concentration of 7.0 mg/L is 744 times larger than that of 2.0 mg/L. CPE is a constant

Table 3
Cyclic potentiodynamic polarization parameters under different oxygen concentration

Samples	O_2 concentration/(mg/L)	E_{corr}(V)	I_{pass}(A/cm^2)	E_b(V)	E_{pro}(V)	v(μm/y)
304SS	7.0	−0.320	2.0×10^{-6}–2.2×10^{-5}	0.300	−0.157	10.1
HEA	7.0	−0.268	1.0×10^{-6}–1.0×10^{-5}	0.384	−0.244	6.5
	4.0	−0.471	1.3×10^{-6}–1.1×10^{-5}	0.288	−0.361	9.1
	2.0	−0.797	4.4×10^{-4}–1.1×10^{-3}	0.258	0.016	3.2×10^3

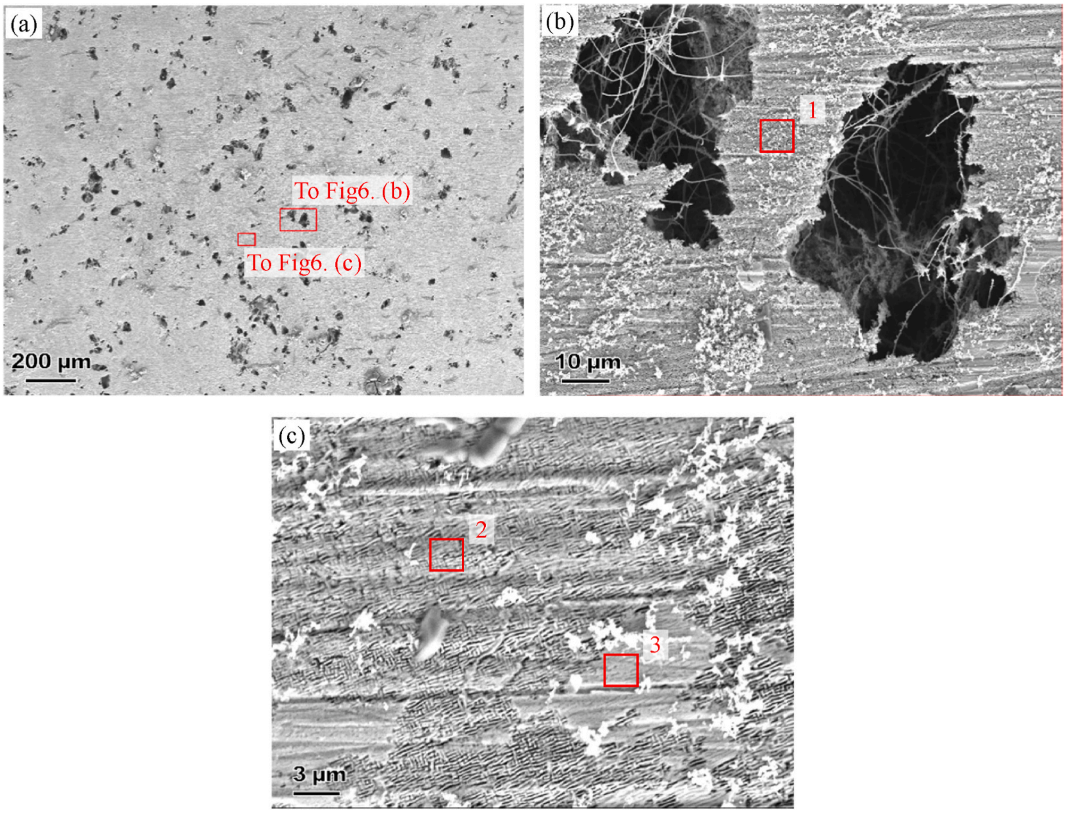

Fig. 6. SEM images of the AlCoCrFeNi after the cyclic potentiodynamic polarization testing at an oxygen concentration of 2.0 mg/L, (a) low resolution, (b) corrosion pits, (c) no corrosion pit position.

phase element, which designates the impedance of a constant phase element as $Z_{CPE} = Y_0^{-1}(j\omega)^{-\theta}$, where Y_0 is the proportionality factor, j is the imaginary unit, ω is the angular frequency, and θ is the phase shift, $-1 \le \theta \le 1$. Z_{CPE} represents an inductance (L), a resistance (R) and a capacitance (C) when $\theta = -1, 0, 1$, respectively [36–44]. As shown in Table 2, where the θ are approaching 1.0. So, $Y_0 \approx C$. Based on the Helmholtz model [45], the adsorptive capacitance is inversely proportional to the thickness of the passivation film (δ) [44–47]:

$$Y_0 \approx \frac{\varepsilon_0 \cdot \varepsilon}{\delta} A \tag{1}$$

Where, ε_0 is the permittivity of a vacuum (8.85×10^{-14} F/cm), ε is the dielectric constant of the passive film, and the A is the surface of the electrode. The values of Y_0 are similar at the oxygen concentration of 7.0 mg/L and 4.0 mg/L, but far less than that at 2.0 mg/L. After corrosion in artificial seawater, the composition on the HEA surface primarily consists of Cr_2O_3, along with small amounts of hydroxides of Fe, Al, and Ni [43]. Based on the inverse relationship between Y_0 and passivation film thickness, the relationships between passivation film thickness and dissolved oxygen concentrations were only qualitatively evaluated. So, it is concluded that the passivation film formed under low oxygen concentration conditions is thinner than that formed under higher oxygen conditions.

In conclusion, under low oxygen conditions, the resistance of the passivation film (R_p) is smaller due to its thinness. Consequently, the thin film offers weaker protection to the sample. As shown in Fig. 3, the Open Circuit Potential (OCP) is more negative compared to high oxygen conditions.

The cyclic potentiodynamic polarization curves of AlCoCrFeNi under different oxygen concentrations are presented in Fig. 5(a).

Table 4
EDS results of the AlCoCrFeNi after corroded with the oxygen concentration of 2.0 mg/L as shown in Fig. 6 (at%)

Position	Al	Co	Cr	Fe	Ni	O
1	1.3	17.3	43.8	25.4	3.3	8.8
2	1.7	19.4	41.1	23.7	5.5	8.7
3	17.8	17.7	18.8	19.6	21.9	4.3

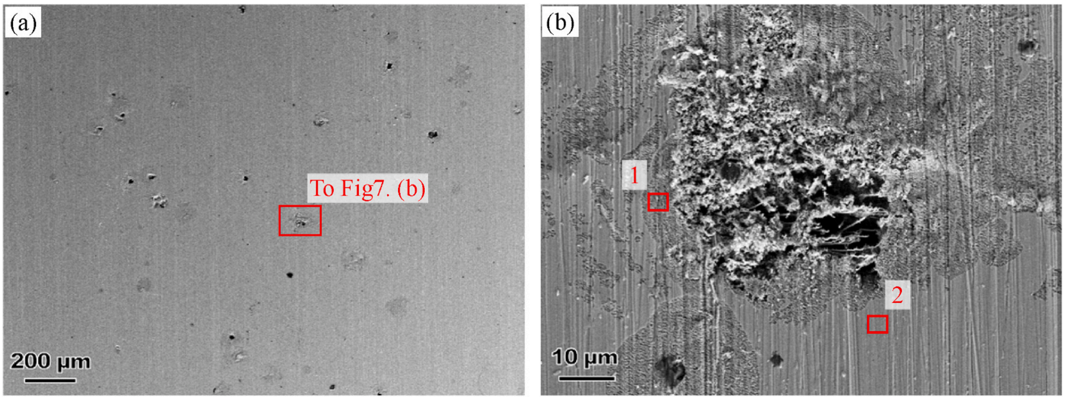

Fig. 7. SEM images of the AlCoCrFeNi after the cyclic potentiodynamic polarization testing at an oxygen concentration of 4.0 mg/L, (a) low resolution, (b) corrosion pit.

Table 5
EDS results of the AlCoCrFeNi after corroded with oxygen concentration of 4.0 mg/L as shown in Fig. 7 (at%)

Position	Al	Co	Cr	Fe	Ni	O
1	1.4	18.8	43.7	24.7	5.8	5.5
2	18.1	20.8	19.2	19.8	22.1	/

The main electrochemical parameters are summarized in Table 3. For comparison purposes, the corrosion parameters of 304SS under the same corrosion conditions with an oxygen content of 7.0 mg/L are also included in Table 3. At 7.0 mg/L, the free corrosion potential (E_{corr}) of 304SS is slightly more negative than that of the high entropy alloy (HEA), and the corrosion rate (v) is slightly higher than that of the HEA. For the HEA, as the dissolved oxygen concentration decreases, besides the free corrosion potential (E_{corr}) decreasing, the breakdown potential (E_b) also decreases. The "breakdown potential" is also referred to as "pitting potential" in any literatures [44,48,49]. However, the anode passivation current density (I_{pass}) increases with the reducing of the oxygen concentration. The I_{pass} at the oxygen concentration 2.0 mg/L is about 400 times larger than that at 4.0 mg/L and 7.0 mg/L.

The protection potential (E_{pro}) is the potential value corresponding to the intersection point of the current-potential curve obtained by reversing the scan (decreasing the potential gradually) after the anode current density suddenly increases and reaches a certain value during the forward scan (increasing the potential gradually) of the steady-state potentiodynamic anodic polarization curve, with the passivation region of the forward scan polarization curve. When the potential is higher than E_b ($E > E_b$), not only does a new corrosion pit form, but the existing corrosion pits also continue to develop. When $E_{pro} < E < E_b$, a new corrosion pit does not form, but the existing corrosion pits continue to develop. When $E < E_{pro}$, no new corrosion pit can be formed, and the existing corrosion pits do not develop either. According to Fig. 5, the E_{pro} value of the AlCoCrFeNi sample at an oxygen concentration of 7.0 mg/L is marginally higher than that at 4.0 mg/L. This suggests that the sample is more prone to undergo repassivation at an oxygen concentration of 7.0 mg/L.

Ignoring concentration polarization, the corrosion rates of the AlCoCrFeNi sample in artificial seawater with varying oxygen concentrations are displayed in Fig. 5(b)–as determined by the Tafel curve extrapolation method. As the oxygen concentration decreases, the corrosion rate increases. It is worth noting that while the corrosion rate increases slightly when the oxygen concentration decreases from 7.0 mg/L to 4.0 mg/L, it experiences a sharp increase when the oxygen concentration further decreases from 4.0 mg/L to 2.0 mg/L. In fact, the corrosion rate at an oxygen concentration of 2.0 mg/L is 421 times higher than that at 7.0 mg/L.

3.3. Microstructure and compositions after corrosion

Fig. 6 is SEM images of the HEA following cyclic potentiodynamic polarization testing at an oxygen concentration of 2.0 mg/L. Numerous corrosion pits are visible on the sample surface. Upon closer inspection of the high-resolution images in Fig. 6(b) and (c), it becomes evident that apart from a handful of areas that remain uncorroded (position 3 in Fig. 6), the microstructure of most other

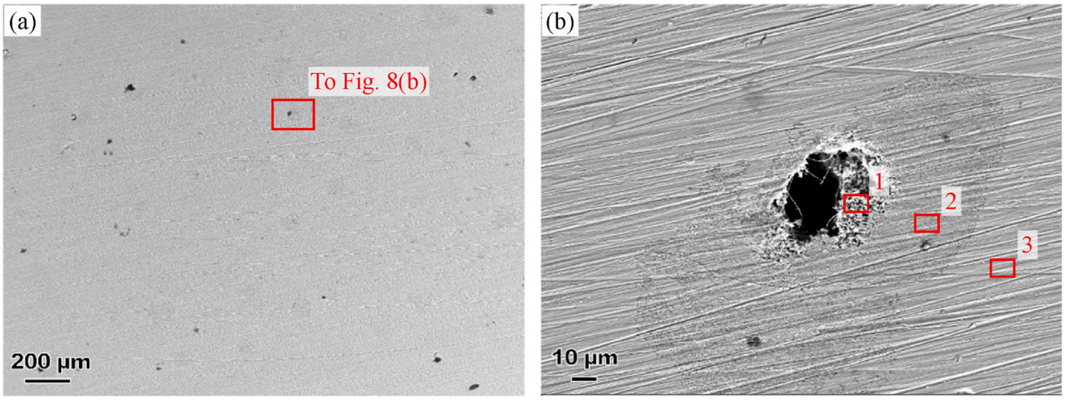

Fig. 8. SEM images of the AlCoCrFeNi after the cyclic potentiodynamic polarization testing at an oxygen concentration of 7.0 mg/L, (a) low resolution, (b) corrosion pit.

Table 6

EDS results of the AlCoCrFeNi after corroded with the oxygen concentration of 7.0 mg/L as shown in Fig. 8 (at%)

Position	Al	Co	Cr	Fe	Ni	O
1	1.2	18.2	46.3	27.3	2.1	4.8
2	1.5	19.1	43.2	24.5	6.7	5.0
3	17.5	19.3	19.6	20.9	22.7	/

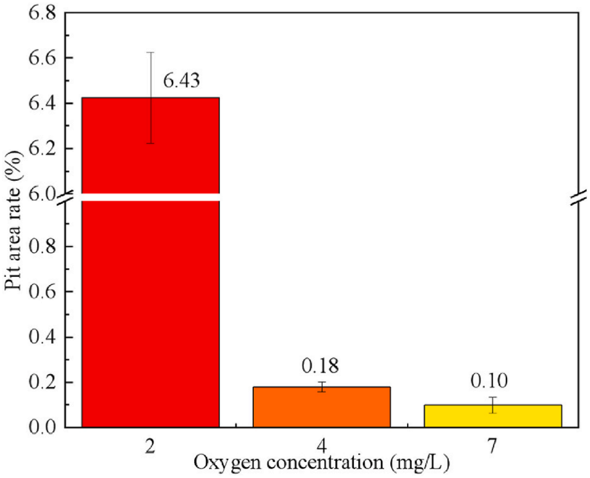

Fig. 9. Relationships between the pit area rate and the dissolved oxygen concentration.

regions, both surrounding and away from the corrosion pits, appears porous (position 1 and 2 in Fig. 6). Table 4 provides the compositions of the different positions in Fig. 6. At the loose microstructure, the Al content (1.3–1.7 %) and Ni content (3.3–5.5 %) are significantly lower than the initial composition (Al: 19.6 %, Ni: 21.0 %). Under low oxygen concentration, the HEA's corrosion form tends to uniform corrosion, which is consistent with the results of a low alloy steel (Ni–Cr–Mo–V) under high hydrostatic pressure [50].

Fig. 7 presents SEM images of the HEA following cyclic potentiodynamic polarization testing at an oxygen concentration of 4.0 mg/L. Numerous corrosion pits also develop on the sample surface. However, only the microstructure surrounding the pits appears loose, where the Al and Ni content (position 1 in Fig. 7) is also lower than the initial composition, as shown in Table 5. Around the loose microstructure, large uncorroded areas can be observed, where the contents of each element (position 2 in Fig. 7) are similar to the initial composition.

Fig. 8 presents SEM images of the HEA following cyclic potentiodynamic polarization testing at an oxygen concentration of 7.0 mg/L. Like the oxygen concentration of 4.0 mg/L, only a few corrosion pits are visible on the sample surface. The microstructure around the corrosion pit is loose, where the Al and Ni content (position 2 in Fig. 8) is lower than the initial composition. It is worth noting that the Ni content within the corrosion pit (position 1 in Fig. 8) is lower than that at the loose microstructure (6.7 at% at position 2 in

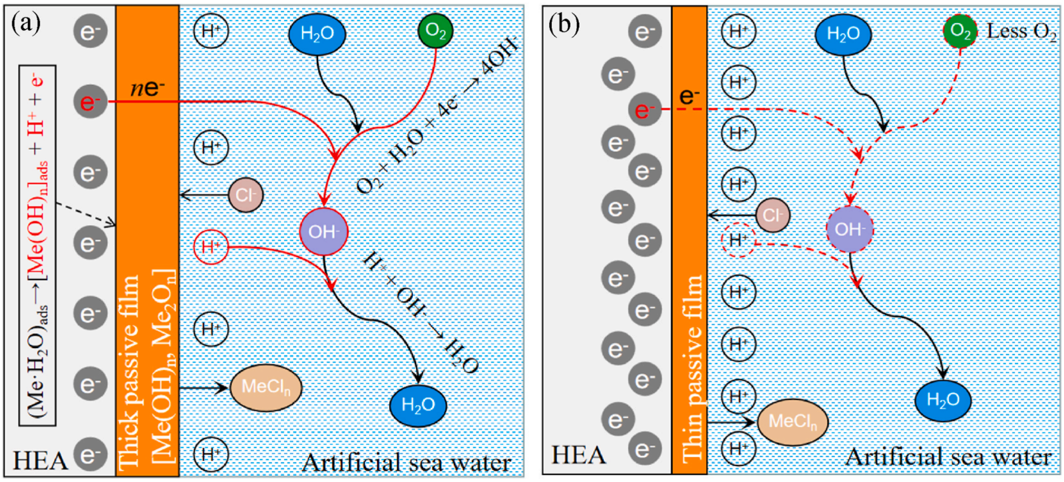

Fig. 10. Diagrammatic drawing of the passivation process with different dissolved oxygen concentration, (a) high oxygen concentration, (b) low oxygen concentration.

Fig. 8).

The "pit area rate" denotes the proportion of the pit opening area on a corroded sample surface to the overall sample surface area. It is observed by comparing Figs. 6–8 and Tables 4–6 that, as the oxygen concentration increases, the pit area rate on a single sample surface decrease. After counting the corrosion pit's area on multiple SEM images, the relationships between the pit area rate and the oxygen concentration are presented in Fig. 9. Under an oxygen concentration of 2.0 mg/L, the pit area rate is 6.43 %, which is significantly larger than that at 4.0 mg/L and 7.0 mg/L.

Second, under low oxygen concentration conditions, corrosion pits and loose microstructure are observed in most places on the HEA surface. However, under high oxygen concentration conditions, only loose microstructure is found around the corrosion pits. This suggests that as the dissolved oxygen concentration decreases in the artificial seawater, the corrosion form of the AlCoCrFeNi alloy changes from pitting to uniform corrosion. The reduction in oxygen concentration may lead to a more uniform distribution of corrosion on the alloy surface, resulting in a transition from localized pitting corrosion to more widespread uniform corrosion.

Third, in the corroded loose microstructure, not only the content of Al reduces, but also the element Ni decreases.

4. Discussion

Although the cast AlCoCrFeNi HEA has a dendrite microstructure, there is minimal difference in element content between the dendrite and interdendrite regions. Therefore, it is considered that the chemical composition of the cast HEA is relatively uniform. When the HEA with a uniform composition is immersed in artificial seawater, metal elements from the alloy dissolve into the solution, and a passivation film forms on its surface. This passivation film acts as a protective layer that can prevent further corrosion of the metal. The dissolved oxygen concentration plays a crucial role in the passivation process, as shown schematically in Fig. 10.

The passivation processes remain similar across various oxygen concentration conditions. At the interface between the HEA and the solution, metal atoms (Me = Al, Co, Cr, Fe, Ni) adsorb water through physical adsorption [35,51]:

$$Me + H_2O \leftrightarrow Me \bullet H_2O_{ads} \tag{2}$$

Then, $Me \bullet H_2O_{ads}$ multiple ionization occurs consecutively:

$$Me \bullet H_2O_{ads} \rightarrow (MeOH)_{ads} + H^+ + e^- \tag{3}$$

$$(MeOH)_{ads} + H_2O \leftrightarrow \left[Me(OH)_n\right]_{ads} + H^+ + e^- \tag{4}$$

$$\left[Me(OH)_n\right]_{ads} \leftrightarrow Me_2O_n + H_2O \tag{5}$$

Where, n is the valence number of the Me to form hydroxide or oxide. According to the double layer model [52], the electrons (e^-) accumulate on the surface of the specimen, while the hydrogen ions (H^+) are attracted to the interface between the specimen and the solution due to electrostatic forces.

At the interface between the passivation film and the solution, the dissolved oxygen captures the electrons that are transmitted from the passivation film, leading to the following reactions [44]:

$$O_2 + e^- \rightarrow O_2^- \tag{6}$$

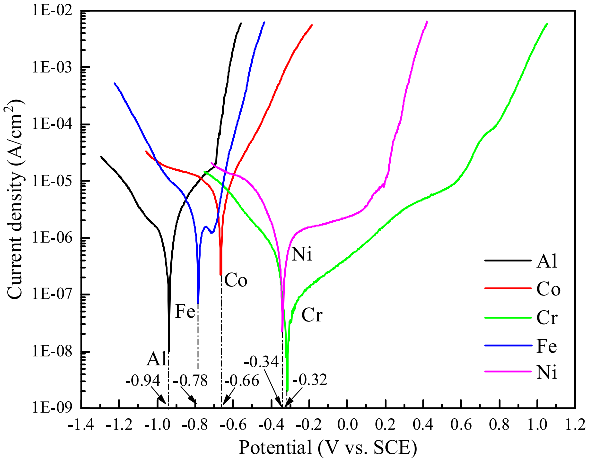

Fig. 11. Potentiodynamic polarization curves of pure metal Al, Co, Cr, Fe and Ni in the artificial seawater with oxygen concentration 7.0 mg/L.

$$O_2^- + H_2O + e^- \rightarrow HO_2^- + OH^- \tag{7}$$

$$HO_2^- + H_2O + 2e^- \rightarrow 3OH^- \tag{8}$$

The combined reaction resulting from reactions (6) through (8) is as follows:

$$O_2 + 4H_2O + 4e^- \rightarrow 4OH^- \tag{9}$$

The OH^- ions generated in reactions (7) and (8) are transmitted to the metal/passivation film interface, where they react with the H^+ ions generated in reactions (3) and (4), ultimately producing water. As a result, hydroxides of the alloy elements are formed on the sample surface. After the hydroxide loses water, a metal oxide film is formed.

According to the phase-forming-film theory [35], the main components of the passivation film are $Me(OH)_n$ and Me_2O_n, as shown in Fig. 10(a). For the HEA AlCoCrFeNi in artificial seawater, the passivation film's main compositions have been reported to be hydroxides of Al, Fe, and Ni, as well as oxides of Al, Fe, Cr, Ni, Co by X-ray photoelectron spectrometer testing in published papers [36].

During the above process, Cl^- and OH^- competitively adsorb with the metal ions in reaction (4). This results in the formation of $MeCl_n$, which dissolves into the solution, disrupting the integrity of the passivation film and accelerating corrosion [4,53,54].

When oxygen concentration is low, as shown in Fig. 10(b), the reactions (6)–(8) are inhibited. This leads to two consequences: First, the electrons generated by reactions (3) and (4) cannot be consumed and accumulate on the HEA surface. Therefore, the sample's OCP and E_{corr} at low oxygen concentration are more negative than those at high oxygen concentration, as evident in Figs. 3 and 4(a).

Second, due to the reduced production of OH^- from reactions (7) and (8), the H^+ generated by reactions (3) and (4) cannot be neutralized. Therefore, the concentration of H^+ increases, which in turn inhibits the reactions (3) and (4). As a result, fewer $Me(OH)_n$ and Me_2O_n are produced on the sample surface. Consequently, the passivation film is thinner and has lower corrosion resistance, as evident in Fig. 4 and Table 2.

Moreover, due to the passivation film which generated in artificial seawater with low oxygen concentration is thin, the film cannot effectively protect the HEA sample. On one hand, more pitting active points will be formed on the sample surface, as shown in Fig. 10 (b); On the other hand, because dissolved oxygen diffuses more difficultly under low oxygen levels, it promotes the formation of a block cell and the cell's autocatalytic process, leading to faster development of metastable pitting into steady-state pitting. As a result, there are more corrosion pitting formed on the sample surface after corrosion testing under low oxygen levels. And the most place on the sample surface are loose, as shown on Fig. 6(c). The corrosion mechanism tends to change to uniform corrosion. As a result, corrosion testing under low oxygen levels leads to the formation of more corrosion pits on the sample surface. Additionally, most of the sample surface becomes loose, as shown in Fig. 6(c). The corrosion mechanism tends to shift towards uniform corrosion. Furthermore, the passivation current (I_{pass}) and corrosion rate at low oxygen levels are higher than those at high oxygen levels due to the thin passivation film. Additionally, the breakdown potential (E_b) at low oxygen levels is slightly lower than that at high oxygen levels.

Under low oxygen concentration (2.0 mg/L) conditions, the high anodic current density suggests that the alloy elements Al and Ni undergo significant dissolution. Consequently, the concentration of ions such as Al^{3+} and Ni^{+} increases in the vicinity of the sample surface. The deposition of their oxides and/or hydroxides onto the specimen surface serves to protect the corroded areas from further corrosion. As a result, the protection-current density curve observed under low oxygen concentration exhibits similarities to that observed under high oxygen concentration conditions. Furthermore, due to the notably higher anodic current density at low oxygen concentration (2.0 mg/L) compared to high oxygen concentrations (4.0 mg/L and 7.0 mg/L), the hysteresis loop is particularly narrow at the lowest oxygen concentration, with the intersection of the curves corresponding to the reverse and forward scan occurring at a relatively more positive potential.

As shown in the EDS results in Figs. 6–8 and Table 4 to Table 6, the element Al content at the loose microstructure is lower than its

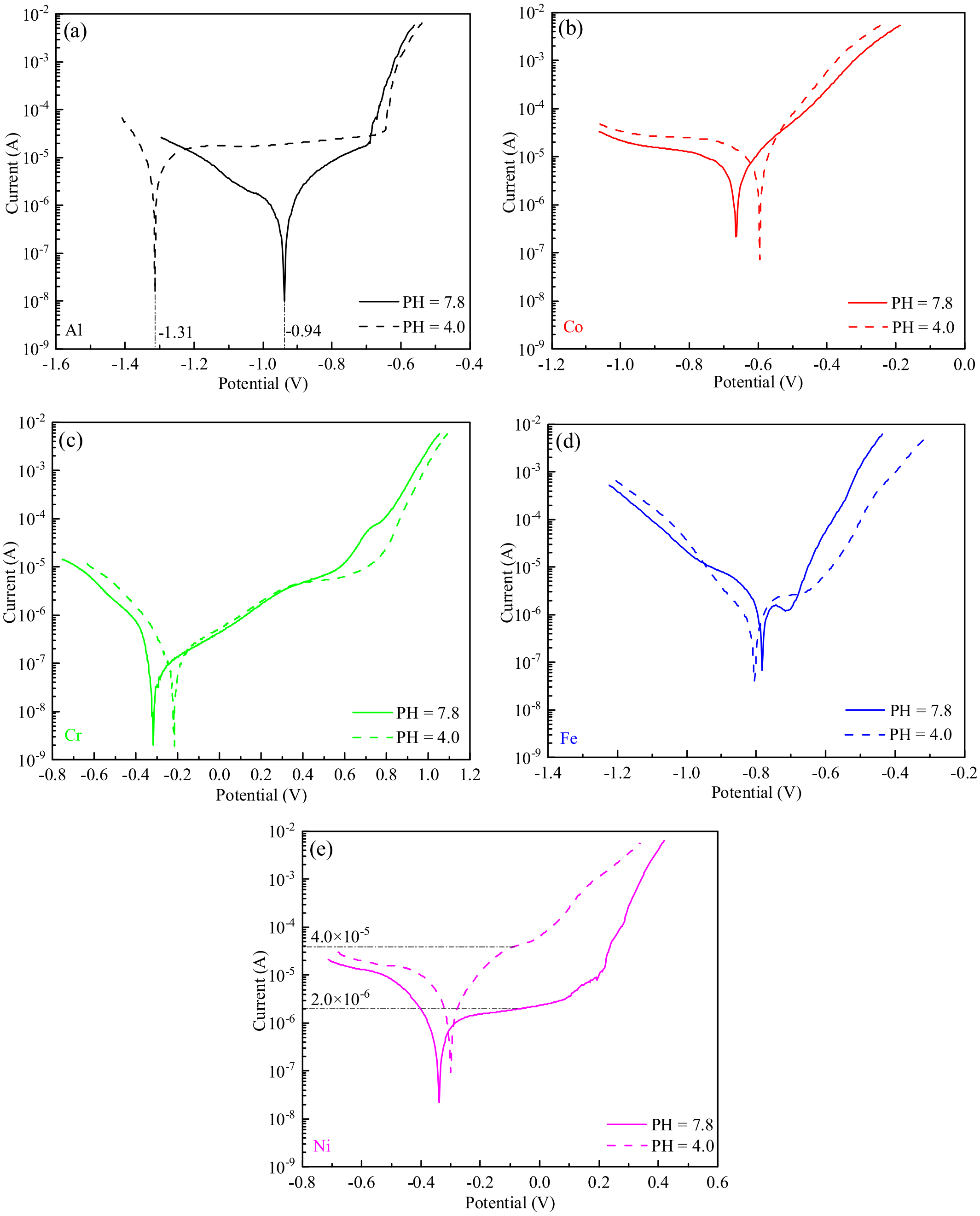

Fig. 12. Potentiodynamic polarization curves of pure metal Al, Co, Cr, Fe and Ni in artificial seawater with an oxygen concentration of 7.0 mg/L and pH values of 4.0 and 7.8, (a) Al, (b) Co, (c) Cr, (d) Fe, (e) Ni.

primordial content. As is well known, when the potential exceeds the breakdown potential (E_b), metal atoms (Me) at the pitting active points begin to dissolve into the electrolyte [35].

$$\mathrm{Me} \rightarrow \mathrm{Me}^{n+} + ne^- \tag{10}$$

$$\mathrm{Me}^{n+} + 4\mathrm{H_2O} \rightarrow \mathrm{Me(OH)}_n \downarrow + n\mathrm{H}^+ \tag{11}$$

It is thought that the alloy element Al is more reactive than other elements in the AlCoCrFeNi alloy, and the element Al preferentially replaces Me in reactions (10) and (11). Therefore, the Al content decreases. To confirm this idea, the potentiodynamic polarization curves of pure metals Al, Co, Cr, Fe, and Ni were tested in artificial seawater with an oxygen concentration of 7.0 mg/L. The results are shown in Fig. 11. Compared to other pure metals, pure Al has the lowest free corrosion potential ($E_{corr} = -0.94$ V vs. SCE)

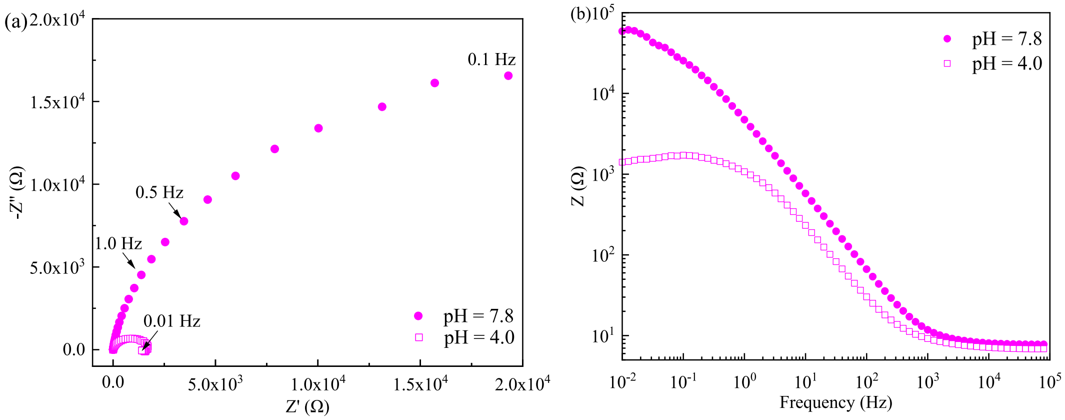

Fig. 13. Electrochemical impedance spectroscopy of the pure Ni in the artificial seawater at an oxygen concentration of 7.0 mg/L with pH = 4.0 and pH = 7.8, (a) Nyquist plots, (b) Bode plots.

and the highest anodic current density. Therefore, the above speculation (Al preferentially dissolves due to its high activity) is confirmed.

In addition to the alloy element Al, the nickel (Ni) content also decreases at the HEA's loose microstructure. However, as shown in Fig. 11, the free corrosion potential of pure Ni in the artificial seawater is high ($E_{corr} = -0.32$ V vs. SCE), which is only slightly lower than that of pure Cr. So, the dissolve mechanism of Ni is different with that of Al. How do we explain this phenomenon?

It is found from reactions (10)–(11) that the H^+ content is high near the pitting active points after the alloy elements Al is dissolved (local acidizing). So, it is hypothesized that the "local acidizing" near the pitting active points leads to the dissolution of alloy element Ni. To confirm this speculation, the potentiodynamic polarization curves of pure metals Al, Co, Cr, Fe, and Ni were tested in artificial seawater with oxygen concentrations of 7.0 mg/L at pH values of 4.0 and 7.8 (adjusted by adding HCl solution). As shown in Fig. 12, the anode passivation current of pure Ni at pH = 4.0 is 20 times larger than that at pH = 7.8. Therefore, it is confirmed that acidification promotes the dissolution of alloy element Ni in artificial seawater. Additionally, it is observed from Fig. 12 that the free corrosion potential (E_{corr}) of pure Al at pH = 4.0 (−1.31 V vs. SCE) is lower by 0.37 V than that at pH = 7.8, which is also the lowest among the five alloy elements at pH = 4.0 in artificial seawater. At pH = 4.0 and pH = 7.8, the free corrosion potential (E_{corr}) of other pure metals (Co, Cr, Fe and Ni) exhibits only small differences (<0.1 V). Moreover, the polarization curves of pure Co, Cr, and Ni display similar shapes under both pH conditions.

Fig. 13 illustrates the electrochemical impedance spectroscopy (EIS) of pure Ni in artificial seawater, with pH levels of 4.0 and 7.8. The Nyquist plots in Fig. 13(a) clearly show that the arc radius of capacitive reactance at pH 4.0 is notably smaller compared to that at pH 7.8. In the Bode plots depicted in Fig. 13(b), it is evident that the impedance value (Z) in the low frequency band is lower at pH 4.0 compared to pH 7.8. Consequently, the passivation film formed on pure Ni in artificial seawater at pH 4.0 offers lesser protection to the underlying matrix than that at pH 7.8. These findings provide additional evidence that the dissolved Ni elements from the surface of AlCoCrFeNi are insufficient to effectively protect the sample from further dissolution in a local acidic environment.

Based on the previous analysis, the increased acidity within the corrosion pit leading to a greater dissolution of Ni atoms into the solution. As a result, as illustrated in Fig. 8(b), the Ni content is not only reduced in the corroded loose microstructure compared to the initial composition, but it is also lower within the corrosion pit (position 1 in Fig. 8) than in the surrounding loose microstructure (position 2 in Fig. 8) of the pitting area.

In summary, it was observed that in artificial seawater with low oxygen concentration, the corrosion mechanism of the HEA (AlCoCrFeNi) alloy transitions from pitting corrosion to general corrosion. Additionally, the alloy elements Al and Ni demonstrate preferential dissolution due to their high activity and "local acidification", respectively. These findings represent the main innovation points of this manuscript.

5. Conclusion

(1) As the decreases of the dissolved oxygen concentration in the artificial seawater, the HEA's free corrosion potential decreases, and its passivation current density and corrosion rate increase. The corrosion rate of the HEA at oxygen concentrate 2.0 mg/L is 421 times larger than that at 7.0 mg/L.

(2) Because the reduction process of the O_2 is inhibited at the interface of the passivation film/solution under low oxygen concentration conditions, the passivation film becomes thin, and the pitting active sites number increase. The corrosion form changes from pitting to uniform corrosion.

(3) Under the simulated conditions of three different dissolved oxygen concentrations in the seep sea, the alloy elements content of Al and Ni at the corroded loose microstructure on the AlCoCrFeNi surface reduce obviously. The reducing of Al caused by its high activity in the artificial seawater. The dissolving of Ni caused by the local acidizing near the active sites and corrosion pits. To design a super corrosion resistance in deep sea, the alloy element Al should be avoided and Ni should be added with caution.

Data availability statement

All data included in this study are available upon request by contact with the corresponding author.

CRediT authorship contribution statement

Junwei Wang: Writing – review & editing, Writing – original draft, Project administration, Investigation, Formal analysis, Conceptualization. **Wenhui Wen:** Data curation. **Fa Xie:** Data curation. **Bo Wu:** Data curation. **Yang Yang:** Formal analysis. **Jun Cheng:** Methodology. **Shilong Zhang:** Data curation. **Xianhui Zhang:** Writing – review & editing, Resources, Investigation.

Declaration of competing interest

All authors of this manuscript declare that we have no known competing financial interests or personal relationships that could have appeared to influence the work reported in this paper.

Acknowledgments

The authors would like to thank the anonymous reviewers for his/her valuable comments.

This work was supported by the Laboratory Open Fund of Xiamen city Marine Corrosion and Smart Protective Materials [grant numbers KL72205]; the Fujian Natural Science Foundation [grant numbers 2023J01780]; the Jimei University Research Fund [grant numbers ZQ2021052]; and the Project of Subsidy Funds for Marine Economic Development in Fujian Province [grant numbers FJHJF-L-2022-20].

References

[1] J. Childs, Geographies of deep sea mining: a critical review, Extr. Ind. Soc. 9 (2022) 101044, https://doi.org/10.1016/j.exis.2022.101044.

[2] W.B. Ma, K.R. Zhang, Y.L. Du, X.W. Liu, Y.J. Shen, Status of sustainability development of Deep-Sea mining activities 10 (2022) 1508, https://doi.org/10.3390/jmse10101508.

[3] S.B. Hu, R. Liu, L. Liu, Y. Cui, F.H. Wang, Influence of temperature and hydrostatic pressure on the galvanic corrosion between 90/10 Cu–Ni and AISI 316L stainless steel, J. Mater. Res. Technol. 13 (2021) 1402–1415, https://doi.org/10.1016/j.jmrt.2021.05.067.

[4] F.L. Sun, X.G. Li, L. Lu, X.Q. Cheng, C.F. Dong, J. Gao, Corrosion behavior of 5052 and 6061 aluminum alloys in deep ocean environment of south China sea, Acta Metall. Sin. 49 (2013) 1219–1226, https://doi.org/10.3724/SP.J.1037.2013.00143.

[5] R.K. Wang, Z.C. Zhu, X.H. Su, K. Mianowicz, H. Jia, K.X. Wu, Slurry pumps in deep-sea mining: a review of numerical and experimental studies, Ocean. Eng. 251 (2022) 111150, https://doi.org/10.1016/j.oceaneng.2022.111150.

[6] R.J.K. Wood, Marine wear and tribocorrosion, Wear 376–377 (2017) 893–910, https://doi.org/10.1016/j.wear.2017.01.076.

[7] R.J.K. Wood, Tribo-corrosion of coatings: a review, J. Phys. D Appl. Phys. 40 (2007) 5502, https://doi.org/10.1088/0022-3727/40/18/S10.

[8] Y.M. Luo, J.H. Yang, X. Li, S. Tan, W. Wang, Z.Z. Luo, G.A. Zhang, J.Y. Zhang, Self-lubricating and wear-resistant and anti-corrosive multi-functional coating technologies applied in tropical marine atmosphere, Tribology 43 (2023) 104–120, https://doi.org/10.16078/j.tribology.2022032.

[9] S.S. Sawant, K. Venkat, A.B. Wagh, Corrosion of metals and alloys in the coastal and deep waters of the Arabian Sea and the Bay of Bengal, Indian J. Technol. 31 (1993) 862–866, https://doi.org/10.1109/33.273704.

[10] R. Venkatesan, M.A. Venkatasamy, T.A. Bhaskaran, E.S. Dwarakadasa, M. Ravindran, Corrosion of ferrous alloys in deep sea environments, Br. Corrosion J. 37 (2002) 257–266, https://doi.org/10.1179/000705902225006633.

[11] F.L. Sun, L. Lu, X.G. Li, K. Xiao, J.S. Wu, S. Wang, Corrosion behavior of N6 and Monel400 nickel alloy in deep sea environment of south China sea, J. Chin. Soc. Corrosion Protect 34 (2014) 165–170, https://doi.org/10.11902/1005.4537.2013.104.

[12] J. Wang, J. Meng, X. Tang, W. Zhang, Assessment of corrosion behavior of steel in deep ocean, Journal of Chinese for corrosion and Protection 27 (2007) 1–7. DOI: JournalArticle/5aea32a4c095d713d8a46924.

[13] J.L. Zhou, X.G. Li, X.Q. Cheng, C.F. Dong, C.W. Du, L. Lu, Research progress on corrosion of metallic materials in deep sea environment, Corrosion Sci. Protect. Technol. 22 (2010) 47–51.

[14] J.H. Lin, Z.H. Dan, J.F. Lu, Y. Ding, Y. Wang, H. Chang, L. Zhou, Research status and prospect on marine corrosion of titanium alloys in deep ocean environments, Rare Met. Mater. Eng. 49 (2020) 1090–1099.

[15] S.P. Qu, Y.S. Yin, Research status and development trend of service materials in deep sea extreme environment, Mater. Sci. Technol. 27 (2019) 1–8, https://doi.org/10.11951/j.issn.1005-0229.20180151.

[16] H. Nady, M.M. El-Rabiei, M. Samy, Corrosion behavior and electrochemical properties of carbon steel, commercial pure titanium, copper and copper–aluminum–nickel alloy in 3.5% sodium chloride containing sulfide ions, Egypt. J. Pet. 26 (2017) 79–94, https://doi.org/10.1016/j.ejpe.2016.02.008.

[17] S. Høibråten, P.E. Thoresen, A. Haugan, The sunken nuclear submarine Komsomolets and its effects on the environment, Sci. Total Environ. 202 (1997) 67–78, https://doi.org/10.1016/S0048-9697(97)00105-8.

[18] T.G. Duan, W.S. Peng, K.K. Ding, W.M. Guo, J. Hou, W.H. Cheng, S.T. Liu, L.K. Xu, Long-term field exposure corrosion behavior investigation of 316L stainless steel in the deep sea environment, Ocean. Eng. 189 (2019) 106405, https://doi.org/10.1016/j.oceaneng.2019.106405.

[19] J.W. Yeh, S.K. Chen, S.J. Lin, J.Y. Gan, T.S. Chin, T.T. Shun, C.H. Tsau, S.Y. Chang, Nanostructured high-entropy alloys with multiple principal elements: novel alloy design concepts and outcomes, Adv. Eng. Mater. 6 (2004) 299–303, https://doi.org/10.1002/adem.200300567.

[20] A. Kumar, M. Gupta, An insight into evolution of light weight high entropy alloys: a review, Metals 6 (2016) 119, https://doi.org/10.3390/met6090199.

[21] T.T. Shun, L.Y. Chang, M.H. Shiu, Microstructures and mechanical properties of multiprincipal component CoCrFeNiTix alloys, Mater. Sci. Eng. A. Struct. Mater. 556 (2012) 170–174, https://doi.org/10.1016/j.msea.2012.06.075.

[22] Y. Fu, C. Huang, C.W. Du, J. Li, C.D. Dai, H. Luo, Z.Y. Liu, X.G. Li, Evolution in microstructure, wear, corrosion, and tribocorrosion behavior of Mo-containing high-entropy alloy coatings fabricated by laser cladding, Corrosion Sci. 191 (2021) 109727, https://doi.org/10.1016/j.corsci.2021.109727.

[23] M.C. Gao, J.W. Qiao, High-entropy Alloys (HEAs), vol. 8, 2018, p. 108, https://doi.org/10.3390/met8020108.

[24] Y.Z. Shi, B. Yang, X. Xie, J. Brechtl, K.A. Dahmen, P.K. Liaw, Corrosion of Al_xCoCrFeNi high-entropy alloys: Al-content and potential scan-rate dependent pitting behavior, Corrosion Sci. 119 (2017) 33–45, https://doi.org/10.1016/j.corsci.2017.02.019.

[25] D. Bi, Y. Chang, H. Luo, et al., Corrosion behavior and passive film characteristics of AlNbTiZrSix high-entropy alloys in simulated seawater environment, Corrosion Sci. 224 (2023) 111530, https://doi.org/10.1016/j.corsci.2023.111530.

[26] S. Zheng, Z. Cai, J. Pu, et al., Passivation behavior of VAlTiCrSi amorphous high-entropy alloy film with a high corrosion-resistance in artificial sea water, Appl. Surf. Sci. 542 (2021) 148520, https://doi.org/10.1016/j.apsusc.2020.148520.

[27] L. Xue, Y. Ding, K.G. Pradeep, et al., Development of a non-equimolar AlCrCuFeNi high-entropy alloy and its corrosive response to marine environment under different temperatures and chloride concentrations, J. Alloys Compd. 928 (2022) 167112, https://doi.org/10.1016/j.jallcom.2022.167112.

[28] A.M.J. Popescu, F. Branzoi, I. Constantin, et al., Electrodeposition, characterization, and corrosion behavior of CoCrFeMnNi high-entropy alloy thin films, Coatings 11 (11) (2021) 1367, https://doi.org/10.3390/coatings11111367.

[29] D. Kim, K. Kim, J. Park, et al., Microstructure and corrosion performance of high-entropy alloy and austenite and super duplex stainless steels in 3.5% NaCl solution, Int. J. Electrochem. Sci. 18 (4) (2023) 100074.

[30] Y.F. Kao, T.J. Chen, S.K. Chen, J.W. Yeh, Microstructure and mechanical property of as-cast, -homogenized, and -deformed AlxCoCrFeNi ($0 \leq x \leq 2$) high-entropy alloys, J. Alloys Compd. 488 (2009) 57–64, https://doi.org/10.1016/j.jallcom.2009.08.090.

[31] Y. Ma, B.B. Jiang, C.L. Li, Q. Wang, C. Dong, P.K. Liaw, F. Xu, L.X. Sun, The BCC/B2 Morphologies in AlxNiCoFeCr high-entropy alloys, Metals 7 (2017) 57, https://doi.org/10.3390/met7020057.

[32] Y.K. Mu, L.B. Zhang, L. Xu, K. Prashanth, N.Z. Zhang, X.D. Ma, Y.F. Jia, Y.L. Xu, Y.D. Jia, G. Wang, Frictional wear and corrosion behavior of AlCoCrFeNi high-entropy alloy coatings synthesized by atmospheric plasma spraying, Entropy 22 (2020) 740, https://doi.org/10.3390/e22070740.

[33] M. Lobel, T. Lindner, T. Mehner, L.M. Rymer, S. Bjorklund, S. Joshi, T. Lampke, Microstructure and corrosion properties of AlCrFeCoNi high-entropy alloy coatings prepared by HVAF and HVOF, J. Therm. Spray Technol. 31 (2022) 247–255, https://doi.org/10.1007/s11666-021-01255-2.

[34] ASTM International, D1141-98 Standard Practice for the Preparation of Substitute Ocean Water, ASTM Int, 2013, pp. 1–3.

[35] F.P. Wang, W.L. Kang, H.M. Jing, Principles and Techniques of Electrochemical Testing, first ed., Chemical Industry Press, Bei Jing, 2006.

[36] T.T. Shun, C.H. Hung, C.F. Lee, Formation of ordered/disordered nanoparticles in FCC high entropy alloys, J. Alloys Compd. 493 (2010) 105–109, https://doi.org/10.1016/j.jallcom.2009.12.071.

[37] Z.E. Liu, Fundamentals of Materials Science, second ed., Northwestern Polytechnical University Press, Xi'an, 2003.

[38] W. Li, P. Liu, P.K. Liaw, Microstructures and properties of high-entropy alloy films and coatings: a review, Mater. Res. Lett. 6 (2018) 199–229, https://doi.org/10.1080/21663831.2018.1434248.

[39] J.Q. Yu, State Atlas of Binary Alloys, first ed., Shanghai Science and Technology Press, 1987. Shang Hai.

[40] W.R. Wang, W.L. Wang, S.C. Wang, et al., Effects of Al addition on the microstructure and mechanical property of AlxCoCrFeNi high-entropy alloys, Intermetallics 26 (2012) 44–51, https://doi.org/10.1016/j.intermet.2012.03.005.

[41] Z.E. Liu, Fundamentals of Material Science, second ed., Northwestern Polytechnical University Press, Xi'an, 2003.

[42] W.J. Qiang, C.J. Wu, Metal Material Science, third ed., Metallurgical Industry Press, Bei jing, 2016.

[43] J.W. Wang, W.H. Wen, J. Cheng, L.Y. Dai, S.Y. Li, X.H. Zhang, Y. Yang, H.X. Li, X.B. Hou, B. Wu, J.H. Wu, Tribocorrosion behavior of high-entropy alloys FeCrNiCoM (M = Al, Mo) in artificial seawater, Corrosion Sci. 218 (2023) 111165, https://doi.org/10.1016/j.corsci.2023.111165.

[44] C.P. Lee, C.C. Chang, Y.Y. Chen, J.W. Yeh, H.C. Shih, Effect of the aluminium content of $Al_xCrFe_{1.5}MnNi_{0.5}$ high-entropy alloys on the corrosion behaviour in aqueous environments, Corrosion Sci. 50 (2008) 2053–2060, https://doi.org/10.1016/j.corsci.2008.04.011.

[45] H. Helmholtz, Studien über electrische Grenzschichten, Ann. Phys. 243 (7) (1879) 337–382, https://doi.org/10.1002/andp.18792430702.

[46] M. Kissi, M. Bouklah, B. Hammouti, M. Benkaddour, Establishment of equivalent circuits from electrochemical impedance spectroscopy study of corrosion inhibition of steel by pyrazine in sulphuric acidic solution, Appl. Surf. Sci. 252 (2006) 4190–4197, https://doi.org/10.1016/j.apsusc.2005.06.035.

[47] P. Schmuki, H. Böhni, J.A. Bardwell, In situ characterization of anodic silicon oxide films by AC impedance measurements, J. Electrochem. Soc. 142 (5) (1995) 1705, https://doi.org/10.1149/1.2048644.

[48] Y.L. Chou, J.W. Yeh, H.C. Shih, The effect of molybdenum on the corrosion behaviour of the high-entropy alloys Co1.5CrFeNi1.5Ti0.5Mox in aqueous environments, Corrosion Sci. 52 (8) (2010) 2571–2581, https://doi.org/10.1016/j.corsci.2010.04.004.

[49] Y. Fu, C. Dai, H. Luo, et al., The corrosion behavior and film properties of Al-containing high-entropy alloys in acidic solutions, Appl. Surf. Sci. 560 (2021) 149854, https://doi.org/10.1016/j.apsusc.2021.149854.

[50] Y.G. Yang, T. Zhang, Y.W. Shao, G.Z. Meng, F.H. Wang, Effect of hydrostatic pressure on the corrosion behaviour of Ni–Cr–Mo–V high strength steel, Corrosion Sci. 52 (2010) 2697–2706, https://doi.org/10.1016/j.corsci.2010.04.025.

[51] H.A. El-Kader, S.M. El-Raghy, Electrochemical kinetics of stainless steel in aerated chloride solutions during wear process, Electrochim. Acta 30 (1985) 841–849, https://doi.org/10.1016/0013-4686(85)80139-0.

[52] A. Allagui, H. Benaoum, O. Olendski, On the Gouy–Chapman–Stern model of the electrical double-layer structure with a generalized Boltzmann factor, Phys. Stat. Mech. Appl. 582 (2021) 126252, https://doi.org/10.1016/j.physa.2021.126252.

[53] T.P. Hoar, D.C. Mears, G.P. Rothwell, The relationships between anodic passivity, brightening and pitting, Corrosion Sci. 5 (1965) 279–289, https://doi.org/10.1016/S0010-938X(65)90614-1.

[54] G.O. Ilevbare, G.T. Burstein, The role of alloyed molybdenum in the inhibition of pitting corrosion in stainless steels, Corrosion Sci. 43 (2001) 485–513, https://doi.org/10.1016/S0010-938X(00)00086-X.